Shape formation in active liquid crystals by topological defects

M2 internship report

Camille Thibault

June 25, 2022

Contents

1 Introduction

A biological system is considered to be an example of an active material because it is composed of units that use chemical energy to sustain, for instance, their own motion [1]. The interactions between these units can give rise to large-scale behavior with no counterpart in passive systems. In particular, a fluid composed of activity-driven polar units can give rise to unusual phenomena such as long-range orientational order in two dimensions, active turbulence at low Reynolds numbers or self-propelled topological defects [2].

Topological defects are often defined as the zeros of an order parameter or in other words as domains in space where the orientation of the units is ill-defined. These topological defects are crucial in morphogenetic processes, and they have been shown to be underlying a broad range of biological functions, such as cell extrusion [3] or Fig. 1, collective cell dynamics [4] or even protrusion formation such as in the now famous example of the *Hydra* [5], and shown in Figs. 2 for *Hydra* and 3 for precursor-muscle cells. However, the mechanistic linkage between these biological processes and topological defects remains poorly understood.

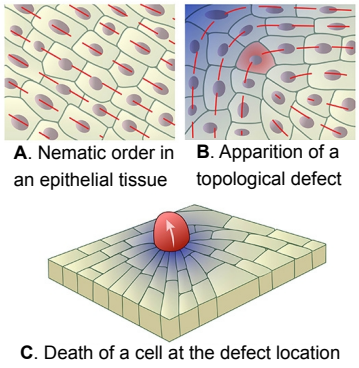

Figure 1: Death of a cell due to the presence of a topological defect (source : B. Ladoux (2017))

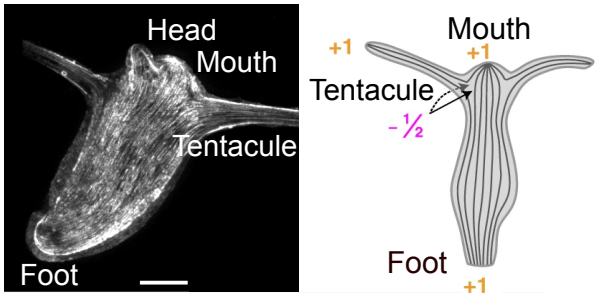

Figure 2: Schematic of the nematic actin fibre organization with topological defects in a mature Hydra. ([5]).

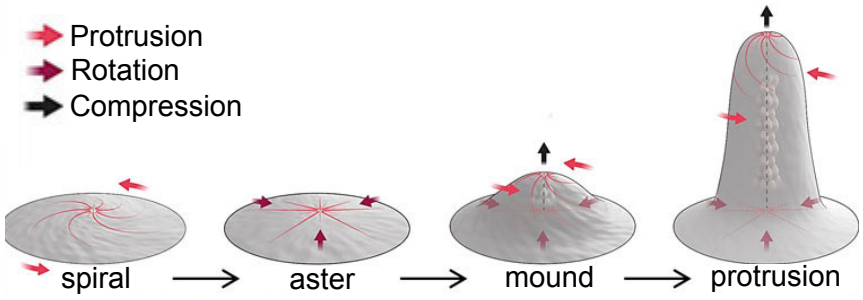

Figure 3: Scheme of the time evolution of cellular nematic architectures from two to three dimensions ([6]). The flows and stress fields are indicated in red and black arrows as indicated in the legend.

Since the seminal work by W. Helfrich and O-Y Zhong-Can [7], who derived the equilibrium and stability conditions of thin layers with surface tension, bending rigidity and volumetric pressure, other authors studied generalisations of this problem, such as [8, 9, 10]. The formation of shapes by topological defects on a surface was first studied in 2008 by R. Frank and M. Kardar [9] for the passive case and recently, extended to an active case by others in for instance [11, 10]. However, recent works by G. Napoli and L. Vergori [12] showed that extrinsic curvature-order couplings, which were not considered in [9, 10], can qualitatively modify the equilibrium behavior of a surface with nematic order. Consequently, there is a need to revisit the problem of shape formation by topological defects at equilibrium and better understand the influence of extrinsic curvature-order couplings.

In this work, we aim at deriving a system of equations solving the equilibrium shape of a thin layer with one topological defect at its center. This work extends [9] by considering the effects of extrinsic curvature-order couplings on the equilibrium problem. We will show that a shape protrusion can emerge as an energy-minimisation process without external forces due to the interplay between surface tension, bending rigidity and orientational order alone. Next, we will express the free-energy for an axisymmetric geometry with an integer topological defect at the center. From the expression of the free-energy and using a linear approximation, we will write the corresponding Lagrangian equations and deduce from them the Hamiltonian and boundary condition for a free-interface. Next, we will retrieve the balance of the normal forces that extents the calculation of [7] for axisymmetric geometries with nematic order and a topological defect. Then, we will study solutions of the system in both the linear and the nonlinear regimes and compare the solutions found in both regimes. Finally, we will investigate the profiles of equilibrium solutions for different sets of parameters and summarise our results in a phase diagram.

2 Theory

In this section, we introduce the free-energy for a thin sheet with components exhibiting nematic liquid-crystal order, called membrane from now on, and we derive its expression for an axisymmetric geometry with an integer topological defect at the axis of revolution in the subsection 2.1. In section 2.2, we derive the

corresponding Lagrangian equations using variational approaches. In section 2.3, we present the boundary conditions used in the present study, and in section 2.4, we linearise the equations with respect to a flat geometry with an integer topological defects at its center to small perturbations.

2.1 Conventions and writing of the free energy

We consider that the free energy of our membrane is:

$$F = \int_{\mathscr{A}} \left\{ \frac{k_c}{2} \mathscr{H}^2 + \frac{K_0}{2} (\partial_\alpha n_\beta)^2 + \lambda \right\} da, \tag{1}$$

where the first term corresponds to the bending energy with bending rigidity k_c and mean curvature $\mathscr{H}$, the second to the Frank free energy with elastic constant K_0 and director field $\mathbf{n}$ and the third to the surface tension with elastic constant λ.

Since the seminal work by W. Helfrich and O-Y Zhong-Can [7], who derived the equilibrium and stability conditions of thin layers with surface tension, bending rigidity and volumetric pressure, other authors studied generalisations of this problem with varying degrees of complexity. For instance, in I.Dérenyi etal [8], the authors included the effects of an external point-like normal force applied to the membrane, and found the formation of tube-like shapes above a threshold. J.R. Frank and M. Kardar [9] were the first to study the effects of topological defects in nematic liquid-crystal order by including intrinsic curvature-order couplings, and found dome-like shapes near integer topological defects. Recent works by LA. Hoffmann, etal [10] extended these ideas to active membranes with intrinsic curvature-nematic order couplings and characterised numerically the dynamics of this problem, finding a range of dynamical phenomena, such as spontaneous emergence of tubes or signatures of a pearl-like instability. Unlike previous works, Eq. (1) includes both extrinsic and intrinsic curvature-order couplings. The latter were, first, found to modify qualitatively the equilibrium physics of membranes with nematic order in G. Napoli and L. Vergori [12]. Below, we detail the main differences with respect to J.R. Frank and M. Kardar work.

Next, we explicit the derivation of the free-energy for axisymmetric geometries with an integer defect. For this geometries, the position of a membrane element can be parametrized by the position vector $\mathbf{r}$:

$$\mathbf{r} = \Big(r(s)\cos(\theta), r(s)\sin(\theta), z(s) \Big) \tag{2}$$

with s being the arc-length and θ the azimuthal angle in cylindrical coordinates, see Fig. 4 for an schematic. We enforce the constraint that the norm of the tangent vector $\partial_s \mathbf{r}$ has to be equal to 1. Allowing us to set $\partial_s r = \cos(\psi(s))$ and $\partial_s z = -\sin(\psi(s))$ where $\psi(s)$ corresponds by convention to minus the angle of the tangent vector of the generatrix in the cartesian plane defined by the radial and axial vectors, as described in Fig; 4

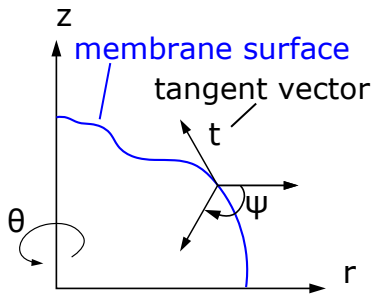

Figure 4: Schematic of the parametrization of a surface of an axisymmetric membrane. The coordinates r, θ and z corresponds to cilindrical coordinates. $\mathbf{t}$ corresponds to the tangent of the generatrix, and ψ is minus the angle of the tangent in the $z-r$ plane.

The partial derivatives of $\mathbf{r}$:

$$\begin{cases} \partial_s \mathbf{r} = (r'(s)\cos(\theta), r'(s)\sin(\theta), z'(s)) \\ \partial_\theta \mathbf{r} = r(s)(-\sin(\theta), \cos(\theta), 0), \end{cases} \tag{3}$$

define an orthogonal base for the tangent plane, which can be normalised by taking $\mathbf{e}_s = \partial_s \mathbf{r}$ and $\mathbf{e}_\theta = \frac{\partial_\theta \mathbf{r}}{r(s)}$. The normal unit vector to the tangent plane is :

$$\hat{n} = (-z'(s)\cos\theta, -z'(s)\sin\theta, r'(s)). \tag{4}$$

For axisymmetric geometries, the metric tensor defined as $g_{\alpha\beta} = \partial_\alpha \mathbf{r} \cdot \partial_\beta \mathbf{r}$ takes the expression :

$$\mathbf{g} = \begin{bmatrix} 1 & 0 \\ 0 & r^2 \end{bmatrix} \tag{5}$$

and the curvature tensor, defined as $\mathcal{C}_{\alpha\beta} = -\partial_{\alpha\beta}\mathbf{r} \cdot \hat{n}$, takes the form:

$$\mathcal{C}^\beta_\alpha = \mathcal{C}_{\alpha\gamma} g^{\gamma\beta} = \begin{bmatrix} \psi' & 0 \\ 0 & -z'r \end{bmatrix}. \tag{6}$$

The inverse of the metric tensor is $\mathbf{g}^{-1} = g^{\alpha\beta}$.

These tensors allow us to determine the element of area as well as the mean and the gaussian curvatures as :

$$\left\{ \begin{array}{lcccc} da & = & |det(g_{\alpha\beta})| ds d\theta & = & r ds d\theta \\ \mathscr{H} & = & -\frac{1}{2}\mathcal{C}^\gamma_\gamma = c_1 + c_2 & = & -\frac{1}{2}\Big(\psi' - \frac{z'}{r}\Big) \\ \mathcal{K} & = & det(\mathcal{C}^\beta_\alpha) = c_1.c_2 & = & -\psi' \frac{z'}{r} \end{array} \right. \tag{7}$$

with the principal curvatures $c_1 = \psi'$ and $c_2 = -\frac{z'}{r}$.

Finally we can compute the director gradient tensor $\partial_\alpha n_\beta$:

$$\begin{aligned} \partial_\alpha n_\beta = & = (\hat{e}_s \partial_s + \frac{\hat{e}_s}{r}\partial_\theta) \otimes (\cos(\xi)\hat{e}_s + \sin(\xi)\hat{e}_\theta) \\ & = \cos(\xi)\hat{e}_s \otimes \partial_s \hat{e}_s + \sin(\xi)\hat{e}_s \otimes \partial_s \hat{e}_\theta + \frac{\cos(\xi)}{r}\hat{e}_\theta \otimes \partial_\theta \hat{e}_s + \frac{\sin(\xi)}{r}\hat{e}_\theta \otimes \partial_\theta \hat{e}_\theta \\ & = -\psi' \cos(\xi)\hat{e}_s \otimes \hat{n} + \frac{\cos(\xi)r'}{r}\hat{e}_\theta \otimes \hat{e}_\theta + \frac{\sin(\xi)z'}{r}\hat{e}_\theta \otimes \hat{n} - \frac{\sin(\xi)r'}{r}\hat{e}_\theta \otimes \hat{e}_s, \end{aligned} \tag{8}$$

where we used the relations $\partial_s \hat{e}_s = -\psi' \hat{n}$, $\partial_\theta \hat{e}_s = r' \hat{e}_\theta$, $\partial_s \hat{e}_\theta = 0$, and $\partial_\theta \hat{e}_\theta = z' \hat{n} - r' \hat{e}_s$. Therefore, up to a scaling factor, the Frank free-energy is :

$$\begin{aligned} (\partial_\alpha n_\beta)^2 & = (\psi' \cos(\xi))^2 + \Big(\frac{\cos(\xi)r'}{r}\Big)^2 + \Big(\frac{\sin(\xi)z'}{r}\Big)^2 + \Big(\frac{\sin(\xi)r'}{r}\Big)^2 \\ & = (\psi' \cos(\xi))^2 + \Big(\frac{r'}{r}\Big)^2 + \Big(\frac{\sin(\xi)z'}{r}\Big)^2 \end{aligned} \tag{9}$$

The difference between J.R. Frank and M. Kardar [9] and ours is that here we consider both the extrinsic curvature terms (corresponding to the normal contributions in Eq. (8)) and the intrinsic curvature terms (corresponding to the rest of the terms in Eq. (8)). In consequence, we found that the Frank free-energy has two more terms as compared to J.R. Frank and M. Kardar, (2008) [9], where the only the term $\Big(\frac{r'}{r}\Big)^2$ in Eq. (9) is considered. These new terms have been found to modify qualitatively the equilibrium behavior of membrane with nematic order in other contexts, in for instance G. Napoli and L. Vergori [12]. In our case, these new terms admit a simple physical interpretation since they can be expressed as a quadratic coupling between the extrinsic curvature tensor $\mathcal{C}$ and the nematic order that is represented by the director field $\mathbf{n}$ (i.e. $\propto (n_\gamma \mathcal{C}^\gamma_\alpha)^2$).

Finally, the expression of the free-energy in this particular configuration is :

$$\begin{aligned} F & = \int (\left[\frac{k_c}{2}\Big(\psi' - \frac{z'}{r}\Big)^2 + \frac{K_0}{2}\Big(\Big(\psi' \cos(\xi)\Big)^2 + \Big(\frac{z'}{r}\sin(\xi)\Big)^2 + \Big(\frac{r'}{r}\Big)^2\Big) + \lambda \right] r \\ & + \gamma\Big(r' - \cos(\psi)\Big) + \eta\Big(z' + \sin(\psi)\Big)) ds \end{aligned} \tag{10}$$

where the two last terms enforce the constraints of our parametrization (i.e. $r' = \cos(\psi)$ and $z' = -\sin(\psi)$) with Lagrange multipliers γ and η.

2.2 Lagrangian equations and Hamiltonian for axisymmetric membranes

Using vairational approaches, one can reduce the search for equilibrium solutions of the free-energy (10) to finding solutions for the fields $\psi(s)$, $z(s)$ and $r(s)$ that satisfy a set of nonlinear differential equation called Lagrangian equations. The variation of a free-energy F with respect to the previous fields reads:

$$\begin{aligned}\delta F &= \int_{S_1}^{S_2} ds \left\{ \left[\frac{\partial \mathcal{L}}{\partial \psi} - \frac{d}{ds}\frac{\partial \mathcal{L}}{\partial \psi'}\right]\delta\psi + \left[\frac{\partial \mathcal{L}}{\partial r} - \frac{d}{ds}\frac{\partial \mathcal{L}}{\partial r'}\right]\delta r + \left[\frac{\partial \mathcal{L}}{\partial z} - \frac{d}{ds}\frac{\partial \mathcal{L}}{\partial z'}\right]\delta z + \frac{\partial \mathcal{L}}{\partial \gamma}\delta\gamma + \frac{\partial \mathcal{L}}{\partial \eta}\delta\eta \right\} \\ &- \left[\mathcal{H}\delta s\right]_{S_1}^{S_2} + \left[\frac{\partial \mathcal{L}}{\partial \psi'}\delta\psi\right]_{S_1}^{S_2} + \left[\frac{\partial \mathcal{L}}{\partial r'}\delta r\right]_{S_1}^{S_2} + \left[\frac{\partial \mathcal{L}}{\partial z'}\delta z\right]_{S_1}^{S_2} = 0 \end{aligned} \tag{11}$$

where $\mathcal{L}(\psi, \psi', r, r', z, z')$ is the Lagrangian and $\mathcal{H}$ is the Hamiltonian. The latter, in our case, reads:

$$\mathcal{L} = \left[\frac{k_c}{2}\left(\psi' - \frac{z'}{r}\right)^2 + \frac{K_0}{2}\left(\left(\psi'\cos(\xi)\right)^2 + \left(\frac{z'}{r}\sin(\xi)\right)^2 + \left(\frac{r'}{r}\right)^2\right) + \lambda\right] r + \gamma\Big(r' - \cos(\psi)\Big) + \eta\Big(z' + \sin(\psi)\Big) \tag{12}$$

which depends explicitly on the fields r, z and ψ and their first derivatives, and the Lagrange multipliers γ and η. Being X a general field, the Lagrangian equation and boundary conditions associated to variations of this field are:

$$\text{In bulk:} \quad \frac{\partial \mathcal{L}}{\partial X} - \frac{d}{ds}\left(\frac{\partial L}{\partial X'}\right) = 0 \tag{13}$$

$$\text{At boundaries:} \quad \frac{\partial \mathcal{L}}{\partial X'} = 0 \tag{14}$$

Below, we detail the expressions of these terms for each of the fields in (12):

$$\frac{\partial \mathcal{L}}{\partial \psi} = \gamma\sin(\psi) + \eta\cos(\psi) \tag{15}$$

$$\frac{\partial \mathcal{L}}{\partial \psi'} = \Big[k_c\Big(\psi' - \frac{z'}{r}\Big) + K_0\psi'\cos^2(\xi)\Big] r \tag{16}$$

$$\frac{\partial \mathcal{L}}{\partial r} = \frac{k_c}{2}\left(\psi'^2 - \left(\frac{z'}{r}\right)^2\right) + \frac{K_0}{2}\Big[\Big(\psi'\cos(\xi)\Big)^2 - \Big(\frac{z'}{r}\sin(\xi)\Big)^2 - \Big(\frac{r'}{r}\Big)^2\Big] + \lambda \tag{17}$$

$$\frac{\partial \mathcal{L}}{\partial r'} = K_0\frac{r'}{r} + \gamma \tag{18}$$

$$\frac{\partial \mathcal{L}}{\partial z} = 0 \tag{19}$$

$$\frac{\partial \mathcal{L}}{\partial z'} = \left[k_c\Big(\psi' - \frac{z'}{r}\Big)\Big(-\frac{1}{r}\Big) + K_0\Big(\frac{z'\sin(\xi)}{r}\Big)\Big(\frac{\sin(\xi)}{r}\Big)\right] r + \eta \tag{20}$$

From these expressions, one can obtain the Lagrangian equations and the expression for boundary conditions (13) and (14). Below, we will derive their explicit expressions in a linear regime.

Because the Lagrangian (12) does not depend explicitly on the arc-length s, the Hamiltonian :

$$\mathcal{H} = -\mathcal{L} + \psi'\frac{\partial \mathcal{L}}{\partial \psi'} + r'\frac{\partial \mathcal{L}}{\partial r'} + z'\frac{\partial \mathcal{L}}{\partial z'} \tag{21}$$

corresponds to a constant (i.e. $\frac{d\mathcal{H}}{ds} = 0$). The expression of the Hamiltonian for our particular case is:

$$\mathcal{H} = r\left(\frac{k_c}{2}(\psi'^2 - \left(\frac{z'}{r}\right)^2) + \frac{K_0}{2}\left[(\psi'\cos(\xi))^2 + (\frac{z'}{r}\sin(\xi))^2 + (\frac{r'}{r})^2\right] - \lambda\right) + \gamma\cos(\psi) - \eta\sin(\psi). \tag{22}$$

When the Frank free-energy vanishes ($K_0 = 0$), Eq. (22) matches exactly the result obtained in [13].

2.3 Boundary conditions

In this work, we will focus on the study of equilibrium shapes for a specific set of boundary conditions. Specifically, we consider that the radial position of the interfaces are fixed, such that $r(s = 0) = 0$ and $r(s = L) = R$, where L is the total length of the generatrix. Besides, we will minimise the total free-energy with respect to variations in the axial coordinate δz and the total length of the generatrix δS. The former

condition implies that $\partial\mathcal{L}/\partial z'$ given by Eq. (20) vanishes at the interfaces, and the latter conditions implies that the Hamiltonian given by Eq. (22) vanishes along the generatrix.

The interpretation of the other boundary conditions related to variations of the angle ψ are unclear near the defect center at $r = 0$, because as it will be illustrated below with some example, in this type of problems one can expect logarithmic divergences at the defect center and in our case, we found these type of divergences for the angle ψ. For this reason, we explicit the last boundary conditions for each specific analysis below, see Sections 3.2.1 and 3.2.2.

2.4 Linear approximation. Small deviations from a flat geometry

Here, we explain the derivation of the equilibrium equations in the limit of small deviations with respect to a flat configuration. In this limit, we consider that the angle $\psi \ll 1$ and that $\psi' \ll 1$ and use the following approximations:

$$z' = -\sin(\psi) \approx -\psi \quad \rightarrow \quad z'' = -\psi'\cos(\psi) \approx -\psi' \tag{23}$$

$$r' = \cos(\psi) \approx 1 \quad \rightarrow \quad r'' = -\psi'\sin(\psi) \sim 0 \tag{24}$$

Note that the previous equation $r' \approx 1$ shows that the arc-length parametrisation s and the radial coordinate r are equivalent when considering small perturbations around a flat configurations. Consequently, from now on we will consider r as the parametrisation variable.

Under these approximation, we can express Eqs. (15)-(20) as:

$$\frac{\partial\mathcal{L}}{\partial\psi} = \gamma\psi + \eta \tag{25}$$

$$\frac{\partial\mathcal{L}}{\partial\psi'} = k_c\Big(r\psi' + \psi\Big) + K_0 r\psi'\cos^2(\xi) \tag{26}$$

$$\frac{\partial\mathcal{L}}{\partial r} = -\frac{K_0}{2r^2} + \lambda \tag{27}$$

$$\frac{\partial\mathcal{L}}{\partial r'} = \frac{K_0}{r} + \gamma \tag{28}$$

$$\frac{\partial\mathcal{L}}{\partial z} = 0 \tag{29}$$

$$\frac{\partial\mathcal{L}}{\partial z'} = -k_c\Big(\psi' + \frac{\psi}{r}\Big) - K_0\Big(\frac{\psi\sin(\xi)^2}{r}\Big) + \eta \tag{30}$$

which allow us to construct the linearized Lagrangian equations:

$$\frac{\partial\mathcal{L}}{\partial z} - \frac{d}{ds}\frac{\partial\mathcal{L}}{\partial z'} = 0 \rightarrow \frac{\partial\mathcal{L}}{\partial z'} = \text{const} = \eta_0 \tag{31}$$

$$\frac{\partial\mathcal{L}}{\partial r} - \frac{d}{ds}\frac{\partial\mathcal{L}}{\partial r'} = \frac{K_0}{2r^2} + \lambda - \gamma' = 0 \tag{32}$$

$$\frac{\partial\mathcal{L}}{\partial\psi} - \frac{d}{ds}\frac{\partial\mathcal{L}}{\partial\psi'} = \gamma\psi + \eta - \Big[\Big(k_c\big(r\psi'' + 2\psi'\big) + K_0(r\psi'' + \psi')\cos^2(\xi)\Big)\Big] = 0. \tag{33}$$

From equations 31 and 32, one can deduce the expressions for γ and η :

$$\eta \;=\; \eta_0 + k_c\Big(\psi' + \frac{\psi}{r}\Big) + K_0\Big(\frac{\psi\sin(\xi)^2}{r}\Big) \tag{34}$$

$$\gamma \;=\; \gamma_0 + \lambda r - \frac{K_0}{2r} \tag{35}$$

where η_0 and γ_0 are integration constants that are set by boundary conditions. Combining these equations with Eq. (33), one obtains a second order differential equation for the angle ψ:

$$\eta_0 + \psi\left(\lambda r - \frac{K_0}{2r} + \frac{k_c}{r} + \frac{K_0\sin(\xi)^2}{r} + \gamma_0\right) - \Big(k_c + K_0\cos^2(\xi)\Big)\big(r\psi'' + \psi'\big) = 0 \tag{36}$$

The linearization of the Hamiltonian (22) takes the form:

$$\mathcal{H} \;\approx\; \gamma_0 - \eta_0\psi. \tag{37}$$

The boundary conditions discussed in Section 2.3 enforce the following constraints:

$$\frac{\partial \mathcal{L}}{\partial z'}\Big|_{s=0,L} = 0 \quad \rightarrow \quad \eta_0 = 0 \tag{38}$$

$$\mathcal{H} = 0 \quad \rightarrow \quad \gamma_0 = 0 \tag{39}$$

$$\tag{40}$$

which leads to a further simplified expression (36)

$$\psi\left(\lambda r - \frac{K_0}{2r} + \frac{k_c}{r} + \frac{K_0 \sin(\xi)^2}{r}\right) - \Big(k_c + K_0\cos^2(\xi)\Big)\big(r\psi'' + \psi'\big) = 0 \tag{41}$$

This is the differential equation that we solved in Section 3.2. The boundary conditions for the angle ψ will be specified in the same section.

3 Results

In this section, we will summarise the main results obtained during the internship. In Section 3.1, we will derive normal forces balance in the presence of extrinsic curvature-order couplings. In Section 3.2, we use the linearised Lagrangian equations with respect to a flat configuration that were derived in Section 2.4 and analyse the conditions of existence for several families of equilibrium solution branches. Finally, in Section 3.3, we explore the nonlinear regime by numerically solving the nonlinear Lagrangian equations that were presented in Section 2.2, and compare the results with the solutions found in the linear regime.

3.1 Normal forces balance

In the seminal work by W. Helfrich and O-Y Zhong-Can [7], the authors derived the exact normal force balance for a thin surface with tension, bending rigidity, and pressure gradients across the surface. This provides a necessary condition for the existence of equilibrium solutions and allows to gain insights on the mechanics of nonlinear membranes. Here, we aimed to generalise their work by including the effects of extrinsic and intrinsic curvature-order coupling through the Frank free-energy in Eq. 1.

For this analysis, we use the linear approximation described in Section 2.4. By differentiating Eq. (41) with respect to s and subsequently diving by r, one obtains:

$$0 = \lambda\big(\psi' + \frac{\psi}{r}\big) + \frac{1}{r^2}\Big(k_c + K_0\sin^2(\xi) - \frac{K_0}{2}\Big)\Big(\psi' - \frac{\psi}{r}\Big) - \Big(k_c + K_0\cos^2(\xi)\Big)\Big(\psi''' + \frac{2\psi''}{r}\Big) \tag{42}$$

$$= \lambda\big(\psi' + \frac{\psi}{r}\big) - k_c\Big[\psi''' + \frac{2\psi''}{r} - \frac{\psi'}{r^2} + \frac{\psi}{r^3}\Big] + K_0\Big[\big(\frac{\sin^2(\xi) - \frac{1}{2}}{r^2}\big)\big(\psi' - \frac{\psi}{r}\big) - \cos^2(\xi)\big(\psi''' + \frac{2\psi''}{r}\big)\Big] \tag{43}$$

Note that the term proportional to λ can be expressed in the form of a Laplace force as :

$$\lambda(\psi' + \frac{\psi}{r}) = -2\lambda\mathscr{H} \tag{44}$$

where the mean curvature $\mathscr{H}$ is given by Eq. (7). This suggests that the other terms in Eq. (43) correspond to the contributions to normal force balance due to bending energy and the Frank free-energy gradients. Equation (43) can be further simplified by applying the Laplace-Beltrami operator to the mean curvature. This operator is defined as :

$$\Delta = \left(\frac{1}{\sqrt{g}}\partial_i\Big(g^{ij}\sqrt{g}\partial_j\Big)\right. \tag{45}$$

where $g = \det(g_{ij})$ and the metric tensor is given by Eq. (7). In our particular case, Laplace-Beltrami operator takes the form

$$\Delta = \frac{1}{r}\Big[\partial_s(r\partial_s) + \partial_\theta\Big(\frac{1}{r}\partial_\theta\Big)\Big] = \frac{1}{r}\partial_r\Big[r\partial_r\Big], \tag{46}$$

and applied to the mean curvature $\mathscr{H}$ reads:

$$\Delta\mathscr{H} = \frac{1}{r}\partial_r\left(r\partial_r\Big(-\frac{1}{2}(\psi' + \frac{\psi}{r})\Big)\right) = -\frac{1}{2r}\partial_r\Big[\psi''r + \psi' - \frac{\psi}{r}\Big] = -\frac{1}{2}\Big[\psi''' + \frac{2\psi''}{r} - \frac{\psi'}{r^2} + \frac{\psi}{r^3}\Big] \tag{47}$$

These results (44) and (47) allows us to rewrite Eq. (43) as :

$$0 = -2\lambda H + 2k_c\Delta H + K_0\Big[\Big(\frac{\sin^2(\xi)-\frac{1}{2}}{r^2}\Big)\Big(\psi' - \frac{\psi}{r}\Big) - \cos^2(\xi)\Big(\psi''' + \frac{2\psi''}{r}\Big)\Big] \tag{48}$$

By comparison to the work of W. Helfrich and O-Y Zhong-Can [7], we identify Eq. (48) as the normal force balance. All the terms in Eq. (48) can be understood easily : the first one is the Laplace force, the second one is the force due to the gradients in bending energy, and the last one is the normal force due to the liquid crystal component. This equation is one of the main results of our work, since it extents the results of previous studies to a general case where both extrinsic and intrinsic curvature-order couplings are considered. This result shows that extrinsic curvature-order couplings, often neglected in previous works, can modify the equilibrium conditions of axisymmetric membranes with nematic order.

3.2 Equilibrium solutions for small perturbations of a flat geometry

The main goal of our project is to identify the families of equilibrium shapes induced by the presence of an integer topological defect on a membrane. In the linear regime that was described in Section 2.4, this corresponds to finding the relations between ψ and z as a function of r. To do so, we have to solve the equilibrium equation (41) with a set of boundary conditions for the angle ψ. We consider that at the outer interface, when $r = R$ being R the radius of the membrane, the angle obeys

$$\frac{\partial\mathcal{L}}{\partial\psi'}\Big|_{r=R} = \Big[k_c\Big(\psi' + \frac{\psi}{r}\Big) + K_0\psi'\cos^2(\xi)\Big]r\Big|_{r=R} = 0 \tag{49}$$

Below, we will discuss in more detail the boundary condition at the center $r = 0$.

Setting the units so that $\lambda = k_c = 1$, the equilibrium shapes only depend on three dimensionless parameters: $(K_0/k_c, \lambda R^2/k_c, \xi)$. Unless stated otherwise, we will set from now on $\xi = 0$. The second parameter will give the maximal value of the radius that will be used to derive $z(r)$. The detailed analytical method that we used for this analysis is explained in Section 4.1

3.2.1 Particular case $\lambda = 0$

Lets first address the problem in a simpler situation, when the tension can be neglected, ie. when $\lambda = 0$. In this case, the general solution is :

$$\psi(r) = c_1\cos[\beta\log(r)] + c_2\sin[\beta\log(r)] \tag{50}$$

with $\beta = \sqrt{(\frac{K_0 - 2k_c}{2K_0 + 2k_c})}$. When $K_0 > 2k_c$, note that the two particular solutions are discontinuous at $r = 0$. This shows that our theory can not describe the physics near the center of the defect. To gain further insights, one can redefine the integrating constant c_2 as a phase or as a scaling factor r_0 :

$$\psi(r) = c_1\cos[\beta\log(r) + \phi_0] = c_1\cos[\beta\log(\frac{r}{r_0})] \tag{51}$$

Now, instead of a physically meaningless integration constant c_2, we can deal with a lengthscale r_0 that can be interpreted. This lengthscale defines a threshold of the radius below which the theory breaks, because the angle ψ is oscillating with a diverging argument. To resolve this ill-defined region $r < r_0$, one would need a theory that accounts for the physics of the core of topological defects, which is much more complicated. In practice, the scale r_0 is set by the microscopic scale of the specific experimental setting. This issue has been discussed in other contexts by P. G. de Gennes and J. Prost [14].

One may also redefine the constants c_1 and c_2, so that the solution $\psi(r)$ reads instead :

$$\psi(r) = \cos[\beta\log(r)] + c_2\sin[\beta\log(r)] \tag{52}$$

Henceforth, for a fix value of c_2, we will use this expression of the angle in order to link it with the general linear solution. Below, we will show that our results do not depend qualitatively on the specific choice for c_2, unless stated otherwise the value of $c_2 = -20$.

3.2.2 General case $\lambda \neq 0$

For the general case, the general solution in the linear regime is :

$$\psi(r) = c_1 \Re\left[f(r)\right] + c_2 \Im\left[f(r)\right]. \tag{53}$$

where

$$f(r) = \text{BesselI}\left(\frac{\sqrt{2k_c + 2 - K_0\cos(2\xi)}}{\sqrt{2k_c + K_0 + K_0\cos(2\xi)}}; \frac{\sqrt{2\lambda}r}{\sqrt{2k_c + K_0 + K_0\cos(2\xi)}}\right)/\text{norm} \tag{54}$$

$$\text{norm} = \frac{2^{-\frac{1}{2}\sqrt{\frac{2k_c - K_0}{2K_c + 2K_0}}}\left(\sqrt{\frac{\lambda}{2k_c + 2K_0}}\right)^{\frac{\sqrt{2k_c - K_0)}}{\sqrt{2k_c + 2K_0}}}}{\Gamma\left(\frac{\sqrt{2k_c - K_0}}{\sqrt{2k_c + 2K_0 +}} + 1\right)} \tag{55}$$

where c_2 is defined such that the Eq. (53) with $c_1 = 1$ matches the solution (52) in the limit $\lambda = 0$.

In order to work with a simpler set of parameters, we define the dimensionless parameters K_0/k_c and $\lambda R^2/k_c$. After fixing the system-dependent parameters ξ to 0, λ and k_c to 1 we still need to find R. Thanks to the boundary condition 49 and depending on the value of K_0, we find different values of R that satisfy the boundary condition, corresponding to different equilibrium solutions. We denote the set of radius R that lead to solutions compatible with the boundary conditions (49) as R_{max}. These different types of solution allow us to build a phase diagram that we will now elaborate further.

3.2.3 Phase diagram and equilibrium solutions

When $K_0/k_c < 2$, there is no value of the radius that satisfy the boundary conditions, and therefore, the system will necessarily be in the flat configuration. For values of $K_0/k_c > 2$, things are getting more complicated and there is an infinity of solutions with values of R_{max} closer and closer to 0, as it was predicted in the simple case where $\lambda = 0$ in Eq. 52. The oscillating divergences at $r = 0$ is recovered in the case when $\lambda \neq 0$. Since too small values of the radius R_{max} may not be relevant in most experimental cases, we will focus on solutions with large values of the radius, (i.e. $\lambda R_{max}/k_c > 0.01$).

Beyond this expected result and for values of K_0/k_c close to the threshold, we found that two new branches appear, Fig. 5, that we will call the "red" branch, closer to 0, and the "green" branch, going to infinity. These two branches emerge at $K_0/k_c = 2.0$ but due to numerical limitations, we were not able to investigate their onset. However, we may observe that the green branch reaches an asymptotic value of $K_0/k_c \approx 2.0334330500822137$ and that the red branch is extended above this asymptote into a "blue" branch, as it can be seen in the inset of Fig. 5.

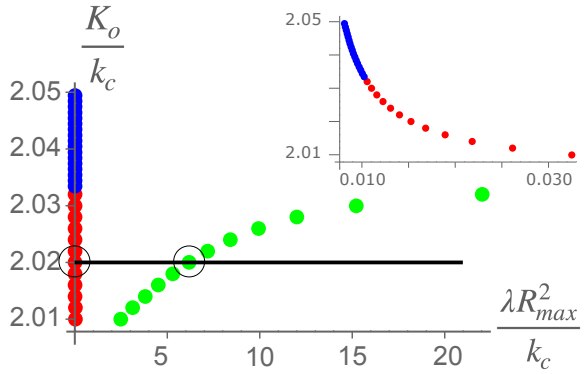

Figure 5: The phase diagram for K_0/k_c between 0 and 2.05. As an inset, see that the red branch extends into the blue branch. The points that are marked in circles and the black line will be studied in the nonlinear regime.

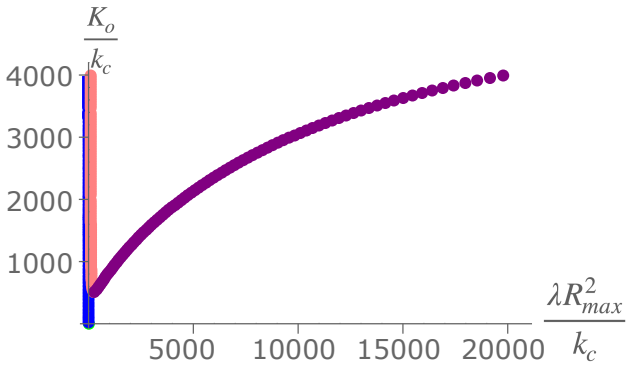

Figure 6: The phase diagram for K_0/k_c between 2.5 and 4000.

For larger values of K_0/k_c, we observe that two new branches of solutions appear at $K_0/k_c \approx 500$, a "pink" one, closer to 0, and a "purple" one for that extents towards infinity, Fig. 6. Remarkably, there is

a region of K_0/k_c where only one (if we don't consider the infinity of branches that exist around 0) branch remains, the "blue" one. In Figure 13, we show that the structure of the phase diagram does not change qualitatively when the value of c_2 in Eq. (53) changes over a broad range of values.

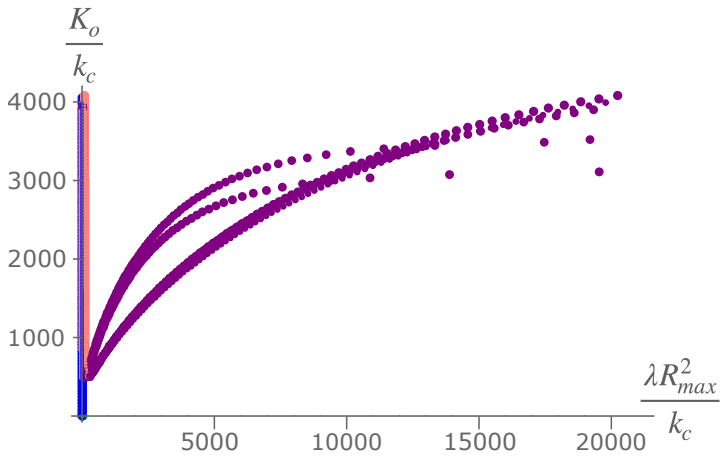

Figure 7: Phase diagrams for K_0/k_c between 2.5 and 4000, when c_2 varies from $-30, -25, -20, -10, 10$, and 20.

Identifying sets of parameters $(K_0/k_c, \lambda R_{max}^2/k_c)$ that satisfy the boundary condition (49) define a set of equilibrium solutions that form branches and can be explicited in a phase diagram is an interesting results.

Next, let's gain further insights on the geometrical properties of these equilibrium solutions. In Figure (5), we explicit and describe several profiles of solutions for varying values of the parameters $(K_0/k_c, \lambda R_{max}^2/k_c)$ that are on a branch of the corresponding colour in Figs. 5 and 6. Notice that we distinguish two different situations for the blue branch (i.e. values of K_0/k_c close and far from the threshold), in order to show its deformation as K_0/k_c increases.

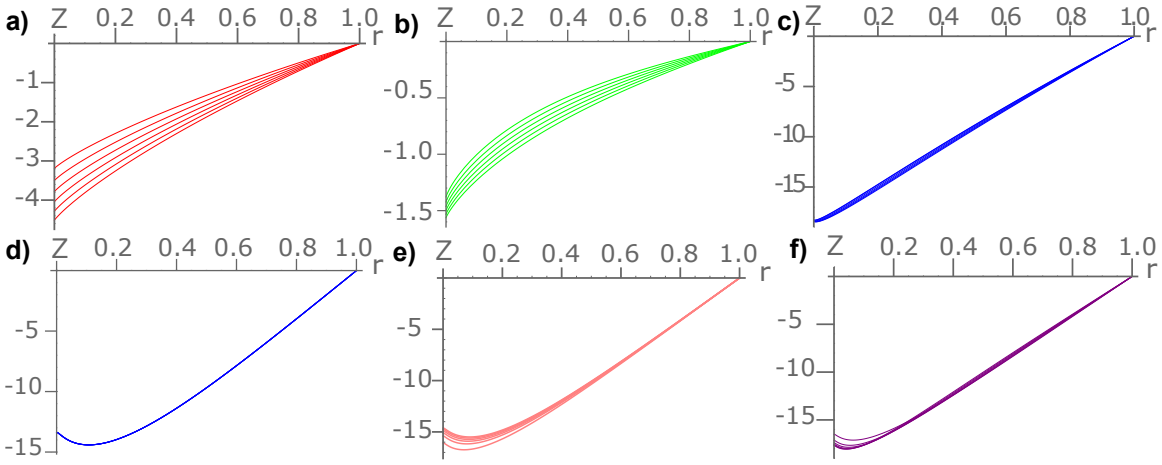

Figure 8: Profile of the solutions for different value of K_0/k_c : a) between [2.01, 2.02] with a step of 0.002, b) between [2.01, 2.02] with a step of 0.002, c) between [3, 11] with a step of 2, d) between [510, 710] with a step of 40, e) between [510, 710] with a step of 40, f) between [510, 710] with a step of 40. The radial coordinate r was scaled by R_{max}.

We found that some of the profiles are more convex (the blue, pink and purple ones) and some of them are more concave (the red and green ones, even if the green one is more arched). In order to have a better idea of what looks like each profile for each branch and to compare them, we can superpose them as shown in Figure (9). We see that the solutions corresponding to smaller values of K_0/k_c are closer to a flat configuration than the other ones. By comparing the blue, pink and purple branches, we see that they tend to be more and more similar.

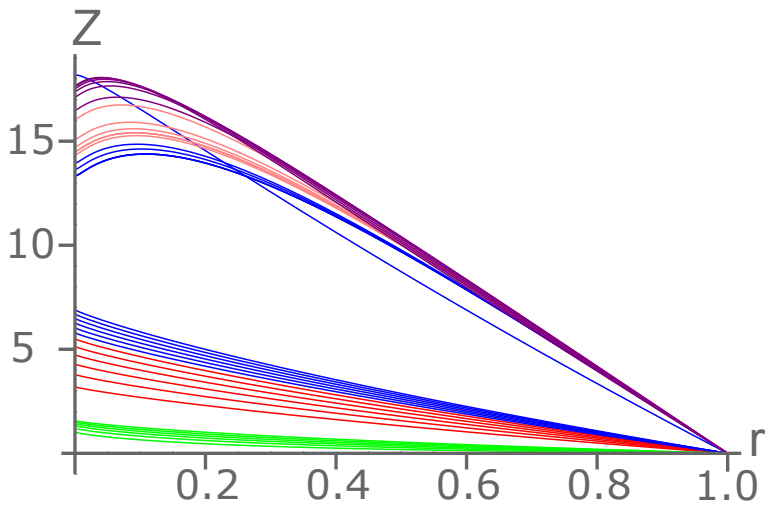

Figure 9: Superposition of all the solutions from the 5 different types of solutions shown in figure (5). As it was shown in figure 5, the red branch extends into the blue branch.

3.3 Nonlinear solutions : comparison with numerical simulations

Until now, we studied analytical solutions of the linearized problem. We identified parameter regimes for different equilibrium solutions, all of them with energies lower than the flat solution one. To investigate further the selection of equilibrium solution, we next relax the linear approximation and explore regimes with nonlinear shape deformations.

Henceforth, we will analyse minimal nonlinear surfaces that are fixed at $r = 0$ and $r = R_{max}$, with the same choices for the boundary conditions as in Section 3.2 (i.e. $\delta\psi \neq 0$, $\delta r = 0$ and $\delta z \neq 0$, meaning $\partial\mathcal{L}/\partial\psi' = \partial\mathcal{L}/\partial z' = 0$ at $r(s_1) = 0$ and $r(s_2) = R_{max}$, see Section 2.2). To achieve this goal, we solve numerically the Lagrangian equations in the general case, and compute the energy associated with the nonlinear solutions $(\psi(s), r(s), z(s))$ that have been found. The detailed numerical method that we use is expanded in Section 4.2.

3.3.1 Study of the profiles

We focused the next analysis to regions with small values of K_0/k_c. First, we computed the nonlinear solutions for a couple of parameter sets $(K_0/k_c, \lambda R_{max}^2/k_c)$ that sits exactly on the branches of the linear solutions, see Fig. 5. In Figs. 10, we found that for the red branch, the linear and nonlinear solutions are in good agreement. This suggests that for values of $(K_0/k_c, \lambda R_{max}^2/k_c)$ that is exactly on the red branch, the optimal shape is the one that is predicted by the linear analysis. In Figs. 11, we found that for the green branch, however, the numerical shape that minimises the energy does not corresponds to the shape of the linear analysis. This suggests that either the linear approximation is inaccurate or that the green branch from Fig. 5 is not an global minimal solution, but rather the red one is.

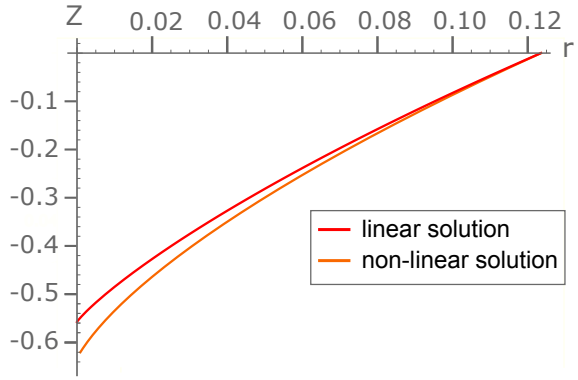

Figure 10: Comparison between the linear and the general solution of the red profile for $(K_0/k_c, \lambda R_{max}^2/k_c) = (2.02, 0.123531)$

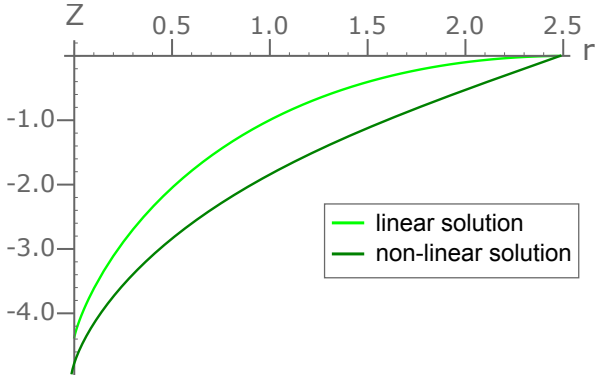

Figure 11: Comparison between the linear and the general solution of the green profile for $(K_0/k_c, \lambda R_{max}^2/k_c) = (2.02, 2.48445)$

Next, we explored the phase diagram for a fixed value of $K_0/k_c = 2.02$ and varying $\lambda R_{max}^2/k_c$. Note that this analysis include parameter values for which no branches were found in the linear analysis, see Fig 5. We found three different types of shapes that are obtained by numerical method. First, we found solutions that are predicted in the linear approximation, as shown in Fig. 1 a) and b). We see that when $\lambda R_{max}^2/k_c$ increases, the shape does not change qualitatively and is always similar to the profile from the red branch in Fig. 5 a). This observation further supports that the red branch corresponds to global minimal shapes, or in other words in the comparison of the linear and the nonlinear solutions Figs. 10 and 11 : the range of stability of the red branch is broader than the green branch, and thus the profiles of "red" type in Fig. 5 a) are dominant at equilibrium. It is possible that profiles of the "green" type in Fig. 5 b) become dominant in parameter regions of the phase diagram that were not explored in this analysis and far away from the red branch. Based on our results, the red solution is always preferred in energy minimization processes, Fig. 1f.

Second, there are some numerical solutions with a total energy less than 40% larger than the flat configuration, as the solutions seen in figure 1 c) and table 1 for the energy values. These solutions do not satisfy the boundary conditions explained in Section 3.3. We believe that they can still be relevant in other contexts and for process that are not constrained by energy minimization.

Finally, the numerical calculation gives also families of highly-deformed configurations, as it can be seen in figures 1 d) and e). These solutions have much larger values of the energy as compared to the flat configuration, table 1. These solutions could arise due to integration errors of our numerical calculations and they are not relevant.

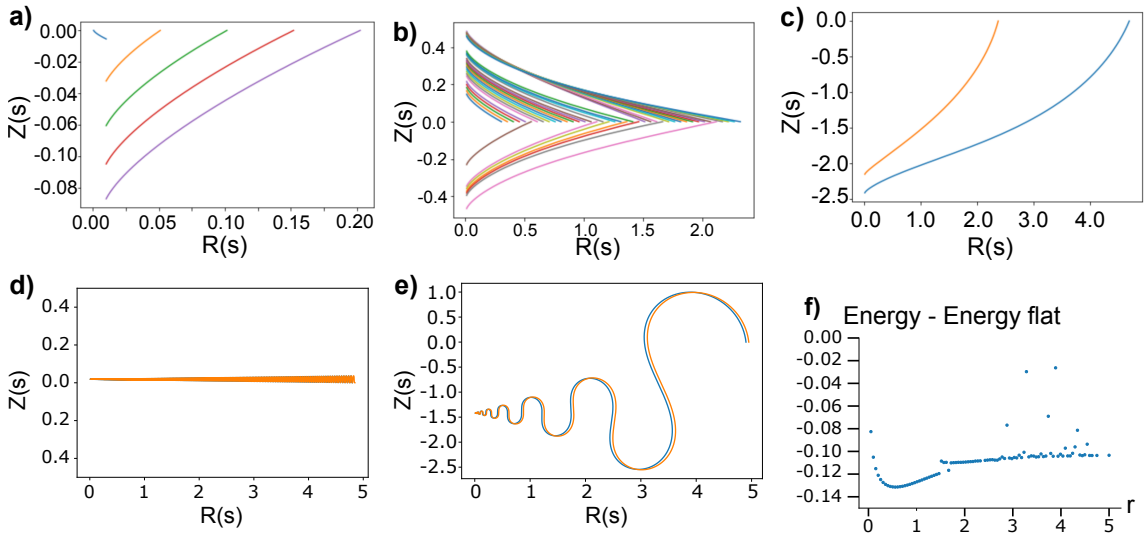

Figure 12: Numerical solutions obtained for $K_0/k_c = 2.02$, a) for small values of $\lambda R_{max}^2/k_c$ between 0.051 and 5.00 b) for values of $\lambda R_{max}^2/k_c$ between 0.2 and 5.0. For some intermediate values of $\lambda R_{max}^2/k_c$ some shapes that were not predicted in the linear approximation, c) dimple-like shapes (R_{max}= 2.374 and 4.697) , d) flat-like configuration that are actually oscillating in very small lenghtscale e) or highly-deformed shapes. (R_{max}= 4.798 and 4.8485) f) Relative energies of the nonlinear solutions in panes (R_{max}= 4.899 and 4.9495) a) and b) with respect to the flat configuration.

Nonetheless, the linear approximation that we performed earlier has proven relevant. Indeed, one may see in figure 1 f) that the energies corresponding to the shapes shown in Fig. 1 a) and b) are always smaller to the flat configuration with the same maximal radii R_{max}, meaning that these configurations are more favoured than a flat membrane. On the contrary, as it is shown in table 1, profiles observed in 1 c), d) and e) have energies greater than their corresponding flat configuration. It means that energetically speaking, the flat configuration will always be preferred. However, one may remark that the solution of type c) that we qualified as physically possible, have much energies more comparable to the flat configuration than the two other shapes.

	c)		d)		e)	
energy	11.15	21.58	2542334.57	2432430.48	457.61	472.08
energy flat	8.34	17.24	17.75	18.00	18.26	18.52

Table 1: Energies corresponding to profiles of figures c), d) and e). The parameters values are indicated in the caption of Fig. 1.

4 Methods

4.1 Description of the Mathematica code

We implemented a Wolfram Mathematica 12.1 program to solve the linear equation 41 analytically.

Using the function DSolve to solve the differential equation 41, we obtain the general solution for $\psi(r)$. In order to be able to manipulate easily the solution we rewrite it in a simpler way, using series expansions and complex notations and obtain the solutions in Eqs. (52) and (53). Then, using the function FindRoot, we determine the radii $\lambda R_{max}/k_c$ that are zeros of the boundary condition (49). Because we are manipulating a system that is sensitive to very small variations, we specified the number of digits to 40 thanks to the option PrecisionGoal in FindRoot. Then, once we have an analytical expression for $\psi(r)$, we may integrate $-\psi$ between 0 and R_{max} to get an expression of $z(r)$, consistently with the linear approximation 23, and using function Integrate. We performed a loop on the values of K_0/k_c for which we want to find the corresponding $\lambda R_{max}/k_c$ and using this method, we were able to specify the phase diagram described in Section 3.2.1 and to study the corresponding profiles 3.3.1.

4.2 Description of the Python code

To solve the nonlinear Lagrangian equations that are obtained from 15-20 and find local energy minima solutions, we used a numerical procedure that was implemented in Python 3.8 program.

After setting the values of the parameters ξ=0 and λ=k_c=1, we choose an arbitrary couple (K_0, R_{max}) to fully specify the parameter values. The range of the space variable s is then specified as $\mathbf{s}$=[0.01,R_{max}]. Remark that it does not start at exactly 0 because as we explained it earlier, the center of the defect is ill-defined, the angle $\psi(s)$ oscillating infinitely at 0.

Then, to integrate the Lagrangian equations, we used a scipy function `scipy.integrate.solve_ivp` with method `Radau` and defining stopping event that prevents the radius to get too close to 0. This function solves an initial value problem for a system of ODE's and therefore takes as an argument a set of initial values for the variables. We want to choose this set of initial values such that the energy is minimised. To do so, we use the scipy function `fmin_powell` that returns the values of $(\psi(s \approx 0), \psi'(s \approx 0))$ that minimise the energy by the Powell's method. This function finds a local minima of a function, which in our case corresponds to the total free-energy (1), by a search in the directions of the function starting from a set of initial guess values. We typically used as initial guess the values (ψ, ψ') from Eq. (52) at ≈ 0 for the set of parameters (K_0, R_{max}).

Finally, using the values that returns this minimisation procedure as initial values for the scipy integration, we solve numerically the Lagrangian equations for the range of s from 0.01 to R_{max}. We check whether the solutions from Fig. 1 satisfy the boundary condition specified in Section 3.3, as shown in Fig. 13 for the branch of minimal shapes:

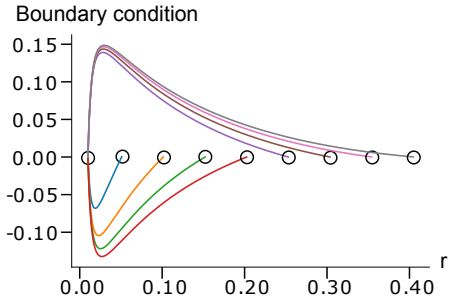

Figure 13: The boundary condition as a function of r for a few non linear solutions. We observe that it always vanishes at 0 and at R_{max}. The position of R_{max} for each solution is indicated with a black circle.

Once the variables (ψ, ψ', r, z) are numerically integrated, one can compute the corresponding energy and to compare it with the energy of a flat configuration with the same radius R_{max}, as we did in 3.3 to obtain for instance the results in Table 1.

5 Conclusion

We studied a thin layer of a nematic liquid crystal when surface tension, bending rigidity and orientational order are considered in the total free energy (Eq.10). We extended previous work by considering both intrinsic and extrinsic order-geometry couplings. We found that this new effects can modify normal force balance, and thus influence the conditions for the existence of equilibrium solutions 48 (Section 3.1). From the total free energy, we derive the corresponding Lagrangian equations using variational approaches 15-20. We solved them analytically by performing a linear approximation for small perturbations of a flat configuration with a topological defect at the center 3.2. This approximation allowed us to find branches of solutions that we represented in a phase diagram, to identify parameter sets for their existence (Section 3.2.3) and to characterise geometrical properties of the shapes associated to each branch (Fig. 5). Then, we solve numerically the problem in the nonlinear general case. We studied specifically a certain region of the phase diagram near instability threshold of the flat configuration and we compared our numerical results with the results from the linear regime (Section 3.3.1). We identified three qualitatively different families of nonlinear equilibrium solutions and discuss some of their characteristics, Fig 1.

It is crucial to understand better the linkage between the formation of shapes and topological defects because they are ubiquitous in morphogenesis 1, [3], [4], [5]. Here, we mainly found the formation of pseudosphere-like shapes like in 1 a) and b), but we found other shapes that it would be interesting to study further, like shapes of the type c)-f) and 1 c). In this work, we could not expand further the study of the phase diagram for bigger values of K_0/k_c due to numerical limitations associated with long convergence times of the optimisation procedure, and it would be the next goal of our work. Some solutions like the profiles in Fig. 1 c) are not predicted by the linear approximation, have an energy bigger than the flat configuration of the same radius and do not satisfy the boundary conditions of a free-interface, however, they might still be relevant solutions in other contexts of biological system, because topological defects can stabilised by the presence of boundaries and energetic preferences are not always favored in biology.

References

[1] Sriram Ramaswamy. The mechanics and statistics of active matter. *Annual Review of Condensed Matter Physics*, 1(1):323–345, 2010.

[2] M. C. Marchetti, J. F. Joanny, S. Ramaswamy, T. B. Liverpool, J. Prost, Madan Rao, and R. Aditi Simha. Hydrodynamics of soft active matter. *Rev. Mod. Phys.*, 85:1143–1189, Jul 2013.

[3] Thuan Beng Saw, Amin Doostmohammadi, Vincent Nier, Leyla Kocgozlu, Sumesh Thampi, Yusuke Toyama, Philippe Marcq, Chwee Teck Lim, Julia M. Yeomans, and Benoit Ladoux. Topological defects in epithelia govern cell death and extrusion. *Nature*, 544(7649):212–216, April 2017.

[4] Kyogo Kawaguchi, Ryoichiro Kageyama, and Masaki Sano. Topological defects control collective dynamics in neural progenitor cell cultures. *Nature*, 545(7654):327–331, April 2017.

[5] Yonit Maroudas-Sacks, Liora Garion, Lital Shani-Zerbib, Anton Livshits, Erez Braun, and Kinneret Keren. Topological defects in the nematic order of actin fibres as organization centres of hydra morphogenesis. *Nature Physics*, 17(2):251–259, November 2020.

[6] P. Guillamat, C. Blanch-Mercader, G. Pernollet, Karsten Kruse, and Aurélien Roux. Integer topological defects organize stresses driving tissue morphogenesis. *Nature Materials*, 21(5):588–597, February 2022.

[7] Ou-Yang Zhong-can and Wolfgang Helfrich. Bending energy of vesicle membranes: General expressions for the first, second, and third variation of the shape energy and applications to spheres and cylinders. *Phys. Rev. A*, 39:5280–5288, May 1989.

[8] Imre Derényi, Frank Jülicher, and Jacques Prost. Formation and interaction of membrane tubes. *Physical Review Letters*, 88(23), May 2002.

[9] John R. Frank and Mehran Kardar. Defects in nematic membranes can buckle into pseudospheres. *Phys. Rev. E*, 77:041705, Apr 2008.

[10] Ludwig A. Hoffmann, Livio Nicola Carenza, Julia Eckert, and Luca Giomi. Theory of defect-mediated morphogenesis. *Science Advances*, 8(15), apr 2022.

[11] Luuk Metselaar, Julia M Yeomans, and Amin Doostmohammadi. Topology and morphology of self-deforming active shells. *Physical review letters*, 123(20):208001, 2019.

[12] Gaetano Napoli and Luigi Vergori. Extrinsic curvature effects on nematic shells. *Phys. Rev. Lett.*, 108:207803, May 2012.

[13] Frank Julicher and Udo Seifert. Shape equations for axisymmetric vesicles: A clarification. *Physical Review E*, 49(5):4728–4731, May 1994.

[14] Pierre-Gilles De Gennes and Jacques Prost. *The physics of liquid crystals*. Number 83. Oxford university press, 1993.